

Exploring the magnetic states in the one-band Hubbard model: Impact of long-range hoppings

Sudip Mandal,¹ Sandip Halder,¹ and Kalpataru Pradhan^{1,*}

¹*Theory Division, Saha Institute of Nuclear Physics,
A CI of Homi Bhabha National Institute, Kolkata 700064, India*
(Dated: March 28, 2025)

Correlated electron systems with competing interactions provide a valuable platform for examining exotic magnetic phases. Theoretical models often focus on nearest-neighbor interactions, although long-range interactions can have a considerable impact on the behavior of the system, creating distinct and complicated magnetic phases. We investigate the consequences of competing interactions in a half-filled one-band Hubbard model on a simple cubic lattice, incorporating hopping processes up to third-nearest-neighbors, to explore the underlying magnetotransport properties. Our magnetic phase diagrams at low temperatures, obtained using semi-classical Monte Carlo analysis, reveal that the long-range interactions can disrupt one form of magnetic phase while creating a new type of magnetic order. For the nonperturbative regime (on-site Hubbard repulsive strength $U \sim$ bandwidth) the C-type antiferromagnetic ground state is preferred over the G-type antiferromagnetic phase when the interaction between second-nearest neighbor sites becomes significant to the nearest-neighbor interactions. However, interactions beyond the second-nearest-neighbors are required to stabilize the A-type antiferromagnetic ground state. Remarkably, at low temperatures, a highly correlated paramagnetic insulating phase develops at the intersection between the antiferromagnetic phases, which might promote a three-dimensional spin-liquid state.

I. INTRODUCTION

Strong electron-electron interactions, a defining feature of correlated electron systems, result in emergent behaviors¹⁻³ that deviate widely from those predicted by traditional band theory⁴. These quantum materials exhibit remarkable phenomena^{1,3} including unconventional superconductivity⁵⁻⁸, huge magnetoresistance^{9,10}, and novel magnetic orderings¹¹⁻¹⁴. In order to comprehend the intricate properties of highly correlated material systems, one needs to analyze complex mechanisms underlying the interplay of strong electron-electron interactions, spin, charge, orbital degrees of freedom, and the underlying lattice structure^{2,15,16}. The understanding of these systems has been enhanced by recent advances in theoretical frameworks such as dynamical mean-field theory (DMFT)¹⁷⁻²⁰, quantum Monte Carlo (QMC)^{18,21-24}, and tensor network approaches²⁵⁻²⁸, as well as experimental techniques like high-resolution spectroscopy^{29,30}, scanning tunneling microscopy^{31,32}, and ultracold-atom simulations³³⁻³⁵.

Investigating the magnetic ordering is essential for identifying a wide range of exotic phenomena in quantum materials^{1,36}. In fact, the onset and suppression of the long-range antiferromagnetic (AF) order are the most studied phenomena in correlated systems^{22,37-42}. Specifically, AF order has been thoroughly examined in materials with rich phase diagrams^{22,38,42} and unusual characteristics^{39,41}, such as cuprates^{43,44}, iron-pnictides^{45,46}, and iron-chalcogenides⁷. Recently, ultracold-atom experiments have become increasingly effective methods for examining AF correlations in controlled settings⁴⁷⁻⁴⁹. These systems enable accurate adjustment of interaction strengths and geometries by simulating the behavior of strongly correlated electrons in optical lat-

tices^{33-35,50}. The identification of antiferromagnetic correlations at low-temperatures in repulsively-interacting Fermi gases^{51,52} is the significant one among the notable accomplishments.

Ongoing research focuses on the impact of competing interactions on the magnetic characteristics and phase diagrams of pristine systems^{39,41,53-55}. These conflicting interactions have the potential to disturb long-range magnetic order and produce new intricate magnetic phases^{39,41,54}. For example, competitive interactions can arise from geometrically incompatible spin alignments, such as those found in triangular^{11,56-60} or Kagome lattices⁶¹⁻⁶³, which may hinder the formation of traditional long-range antiferromagnetic order and instead result in exotic states like non-collinear spin arrangements or spin liquids. Long-range interactions in non-frustrated systems can lead to complicated phase boundaries with competing magnetic ordering, creating intricate phase diagrams^{37,39,41,64}. Actually, second-nearest-neighbor interactions have a major impact on how the charge, spin, and orbital degrees of freedom interact in transition metal-based oxide materials^{37,44,65,66}.

As a fundamental framework for studying and assessing various approaches that characterize different kinds of correlated electron systems, the Hubbard model continues to be of interest⁶⁷⁻⁶⁹. It is particularly helpful for understanding phenomena like magnetism and metal-insulator transitions^{22,42,70,71}. Therefore, despite its seemingly simple specification, the model provides a versatile platform for examining the emergence of intricate collective phenomena that are influenced by temperature, band structure, interaction strength, and electron filling^{39,41,42,72}. These phenomena are caused by the complex interaction of correlations and ordering tendencies, which can compete or cooperate in fascinating ways.

While nearest-neighbor interactions are frequently highlighted in theoretical approaches, the addition of second and third nearest-neighbor interactions can have a significant impact on the dynamics of the system, adding new phases and enhancing the complexity of its phase diagrams^{38,39,64,73}. In fact, long-range hopping processes in the Hubbard model may provide a more thorough and potentially realistic description of some specific materials.

The ground state features are changed when electrons are allowed to hop to second-nearest-neighbor sites because this creates competition between nearest and second-nearest-neighbor hoppings^{38,39,41,73}. For instance, in relation to the half-filled Hubbard model, nearest-neighbor interactions typically favor G-type AF ordering whereas the second-nearest-neighbor interactions disrupt G-type antiferromagnetic order, causing spin rearrangement. As a result, the C-type antiferromagnetic arrangement may be preferred over the G-type antiferromagnetic state when the interaction between the second-nearest-neighbor spins becomes significant. At the same time, interactions beyond the second-nearest-neighbors are necessary to stabilize the A-type antiferromagnetic ground state³⁹. The strength of the long-range hopping parameters, therefore, determines the particular kind of magnetic order that is seen as the ground state. However, these conflicting interactions can also create a situation where exchange interactions can not be satisfied at the same time, resulting in the emergence of a correlated paramagnetic insulating state^{39,64,74} at low temperatures. The combination of paramagnetic insulating state and long-range interactions creates conditions that are favorable for the creation of spin liquid states^{39,64}.

Although long-range interactions typically weaken with distance, they nevertheless have a significant impact on the properties of the system. However, the understanding of the magnetotransport features of the half-filled Hubbard model with long-range interactions in three dimensions remains limited. In this work, we examine how crucial second- and third-nearest-neighbor interactions are in promoting magnetic transitions in the context of highly coupled electron systems. On a simple cubic lattice, we concentrate on the t - t' - t'' based Hubbard model, a paradigmatic approach that includes hopping amplitudes for generating nearest (t), second-nearest (t'), and third-nearest-neighbors (t'') interactions. We investigate the competition among t , t' , and t'' that causes frustration, modifies band structures, and affects the magnetotransport characteristics of the systems by systematically adjusting the respective strengths of these hopping parameters. In order to examine the ground states and their changes in relation to temperature (T) and Hubbard interaction strength (U), we use a well-developed semi-classical Monte Carlo (s-MC) method^{41,42,75–77}. We mainly focus on the nonperturbative regime ($U \sim$ bandwidth) in our study. The nearest-neighbor interaction establishes the G-type AF phase, while the second-nearest-neighbor interaction disrupts it and sets up the C-type

AF phase although the insulating nature remains intact. In addition, our calculations show that the combined effect of three types of hoppings (t , t' , and t'') stabilizes the A-type AF ground state. Remarkably, a small but finite paramagnetic insulating region emerges from the combined action of the first-, second-, and third-nearest-neighbor interactions at the junction of the three types of magnetic ground state phases which can potentially host a spin-liquid phase.

This paper is organized as follows: In Sec. **II**, we outline the model Hamiltonian, long-range hopping parameters, and numerical technique. Appendix **A** provides more information on the model Hamiltonian. In Appendix **B**, we outline the calculation of various physical observables used to investigate magnetotransport properties. At first, we briefly discuss about the magnetotransport properties of the reference Hubbard model in Sec. **III**. Next, we focus on how the second-nearest interaction affects the system's magnetotransport features in Sec. **IV**. The combined effect of the second- and third-nearest-neighbor interactions is then investigated in Sec. **V**. At the end, we present a summary of our results in Sec. **VI**.

II. MODEL HAMILTONIAN AND METHOD

We explore the ground state magnetic phases for the following one-band Hubbard Hamiltonian:

$$\begin{aligned}
 H &= -t \sum_{\langle i,j \rangle, \sigma} c_{i,\sigma}^\dagger c_{j,\sigma} - t' \sum_{\langle\langle i,j \rangle\rangle, \sigma} c_{i,\sigma}^\dagger c_{j,\sigma} - t'' \sum_{\langle\langle\langle i,j \rangle\rangle\rangle, \sigma} c_{i,\sigma}^\dagger c_{j,\sigma} \\
 &\quad + U \sum_i n_{i\uparrow} n_{i\downarrow} - \mu \sum_i n_i \\
 &= H_0 + H_I
 \end{aligned} \tag{1}$$

where t , t' , and t'' are the nearest-neighbor, second-nearest-neighbor, and third-nearest-neighbor hopping parameters, respectively. $\langle \rangle$, $\langle\langle \rangle\rangle$, and $\langle\langle\langle \rangle\rangle\rangle$ correspond to the first-, second-, and third-nearest-neighbor sites, respectively. $c_{i,\sigma}$ ($c_{i,\sigma}^\dagger$) represents the fermion annihilation (creation) operator with spin σ at site i . n_i ($= \sum_\sigma c_{i,\sigma}^\dagger c_{i,\sigma}$) is the number operator. U (> 0) represents the strength of on-site repulsive Hubbard interaction. μ is the chemical potential, which controls the overall average density of the system. For $t' = 0$, the spectrum is particle-hole symmetric and μ turns out to be zero for half-filled case. However, in the same half-filled case, μ becomes finite for nonzero t' and t'' . In our definitions, H_0 represents the non-interacting quadratic part of the model Hamiltonian, whereas H_I containing the interacting quartic term. Our model Hamiltonian calculations are based on the simple cubic lattice that includes periodic boundary conditions.

To solve the model Hamiltonian, we decompose the interacting quartic term (H_I) of the model Hamiltonian by

implementing the standard Hubbard-Stratonovich transformation by introducing Hubbard-Stratonovich (HS) auxiliary fields (\mathbf{m}_i and ϕ_i) at an arbitrary site i . This allows us to employ the semi-classical Monte Carlo (s-MC) approach to simulate the Hamiltonian. In this decomposition, the vector auxiliary field (\mathbf{m}_i) couples with the spin degrees of freedom, while the scalar auxiliary field (ϕ_i) couples with the charge degrees of freedom. Next, we consider the auxiliary fields to be time-independent and treat them as classical fields. We set the scalar field ϕ_i to be proportional to the average density $\langle n_i \rangle$ and define $i\phi_i = \frac{U}{2} \langle n_i \rangle$ at the saddle-point level. However, the auxiliary fields are thermally fluctuating and spatially inhomogeneous, which is the hallmark of our model to capture phases at finite temperatures. Here, it is important to note that the HS transformation is a local transformation that decouples the many-body on-site interaction. Using these approximations (for details, see appendix A), we obtain the following effective spin-fermion Hamiltonian^{42,75,78,79}:

$$H_{eff} = H_0 + \frac{U}{2} \sum_i (\langle n_i \rangle n_i - \mathbf{m}_i \cdot \boldsymbol{\sigma}_i) + \frac{U}{4} \sum_i (\mathbf{m}_i^2 - \langle n_i \rangle^2) - \mu \sum_i n_i, \quad (2)$$

where H_0 represents the hopping terms of the Hamiltonian.

We solve the effective Hamiltonian (H_{eff}) using the exact diagonalization based s-MC technique. In this approach, we diagonalize the Hamiltonian for a fixed configuration of auxiliary fields $\{\mathbf{m}_i\}$ and average charge densities $\{\langle n_i \rangle\}$. At a fixed temperature, the auxiliary fields $\{\mathbf{m}_i\}$ are annealed by employing the Metropolis algorithm. For a fixed temperature, we use 2000 Monte Carlo system sweeps for annealing: first half of the MC sweeps are used to thermally equilibrate the system and the rest MC sweeps are used for measuring the physical observables. During annealing, the average electron densities $\{\langle n_i \rangle\}$ are updated self-consistently at every 10th Monte Carlo step. The main objective of this process is to generate an equilibrium configuration of the auxiliary fields \mathbf{m}_i and the average electron densities $\langle n_i \rangle$. μ is also evaluated self-consistently during the Monte Carlo sweeps to ensure that the system remains at half-filling. Then, we calculate the expectation values of the observables using the eigenvectors and eigenvalues, obtained from diagonalizing the Hamiltonian in equilibrium configuration. These individual expectation values from the equilibrium configurations are further averaged over the results from 100 such configurations at a fixed temperature. All observables are determined by averaging the values obtained from individual configurations. It is important to note that we calculate observables from every 10th equilibrium configuration in order to avoid spurious self-correlations. The temperature is gradually lowered in small steps to allow for equilibration. To overcome size limitations, we employ the Monte Carlo technique

within a traveling cluster approximation (TCA)^{42,79–82} to handle system sizes of $L^3 = 10^3$, where L is the length of the sides of the simple cubic lattice. To ensure consistency, throughout our s-MC study, we assume $t = 1$ and t', t'' are expressed with respect to t . We also express U, T (temperatures) in units of t .

We compute a number of physical observables in order to understand the finer details of the magnetotransport characteristics. To study magnetic features like magnetic transition, we calculate local moments M and quantum correlations using the structure factor $S(\mathbf{q})$. Additionally, we compute temperature-dependent specific heat C_v in order to correlate the low temperature peak structure observed in C_v with the magnetic transition. Transport quantities are investigated by calculating resistivity ρ [inverse of the dc limit of conductivity $\sigma(\omega)$] and density of states (DOS). The appendix B provides an outline of the definitions of the different observables.

III. BRIEF DESCRIPTION OF THE MAGNETOTRANSPORT PROPERTIES OF THE REFERENCE HUBBARD MODEL ($t' = 0$ AND $t'' = 0$)

First, we briefly address the physics of the reference Hubbard model without long-range hoppings (i.e., $t' = 0$ and $t'' = 0$) before looking into the new phenomena observed for $t' \neq 0$ and/or $t'' \neq 0$ cases. We illustrate the U - T phase diagram for the reference model in Fig. 1(a). At low temperatures, the ground state displays a G-type AF insulating phase for all U values similar to previous results in 3D^{18,22,83}. Importantly, the Neel temperature (T_N) behaves non-monotonically as a function of U , as discussed in earlier works using various techniques^{20,22,75}. The G-type AF insulating phase persists even at $U \rightarrow 0$ limit although the resulting T_N is very small. The T_N rises with U until $U = 8$, then decreases as U increases. For $U < 8$, the long-range G-type AF insulating phase transits directly to the paramagnetic metallic phase as the temperature increases. So, the metal-insulator transition temperature (T_{MIT}) coincides with T_N . For $U \geq 8$, a paramagnetic insulating (PM-I) phase separates the G-type AF and Paramagnetic metallic phases. This PM-I phase is characterized by preformed local moments, where the thermal fluctuations suppress long-range order⁷⁵.

For the analysis of magnetic and transport properties, we use $U = 6$ and $U = 12$, from the two distinct regimes in the U - T phase diagram. $U = 6$ and $U = 12$ also correspond to $U/BW = 0.5$ and 1, respectively, where BW denotes the non-interacting bandwidth. Figures 1(b) and (c) show the temperature dependence of the magnetic structure factor $S(\pi, \pi, \pi)$ and resistivity ρ for $U = 12$ and $U = 6$, respectively. For $U = 12$, the T_{MIT} exceeds the T_N significantly. Additionally, we depict the temperature dependence of the specific heat C_v for $U = 12$ in Fig. 1(b) to demonstrate that the T_N and the low temper-

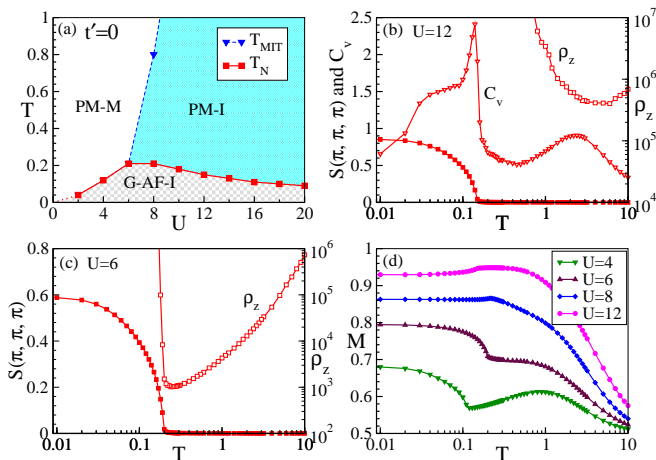


FIG. 1: A brief description of the magnetotransport properties of the reference Hubbard model ($t' = 0$ and $t'' = 0$): (a) The U - T phase diagram: The system shifts directly from a paramagnetic metallic (PM-M) state to a G-type AF insulating (G-AF-I) state for $U < 8$ when the temperature decreases in this regime. For $U \geq 8$, a paramagnetic insulating (PM-I) phase exists between the PM-M and G-type AF insulating phases. (b) Plots of $S(\pi, \pi, \pi)$ vs T and ρ_z vs T demonstrate that for $U = 12$ (\sim bandwidth) the T_{MIT} is greater than T_N , resulting in a PM-I region between the G-type AF insulating and PM-M phases, as illustrated in (a). While the low temperature peak in the specific heat (C_v) signifies the onset of long-range magnetic ordering in the system, the high temperature peak, which is a marker of local moment formation, coincides with the metal-insulator transition temperature (T_{MIT}). (c) For $U = 6$, $S(\pi, \pi, \pi)$ versus T and ρ_z vs T show that the magnetic transition and the MIT happen at the same temperature, i.e. $T_N = T_{MIT}$. (d) As the temperature decreases, the local magnetic moment M increases. For $U \geq 8$, M saturates at low temperatures, with a minor peak around T_N . For lower U values M initially remains relatively steady (for $U = 6$) or drops (for $U = 4$) from $T \approx 1$ to $T \approx T_N$, before increasing below T_N .

ature ($T \sim 0.2$) peak related to spin-fluctuations correspond well to each other. The moment formation and the T_{MIT} are related to the high temperature peak (around $T = 1$) in C_v associated with charge-fluctuations. In general, for the $U = 12$ case, an intervening paramagnetic insulating region separates the PM-M and AF-I phases. On the other hand, Fig. 1(c) illustrates that for $U = 6$, the T_N and the T_{MIT} are comparable. To analyze the relation between magnetic and transport properties further we plot the local magnetic moment (M) as a function of temperature in Fig. 1(d). As the temperature decreases for $U = 8$, the magnetic moment M increases and saturates at low temperatures. It also displays a small peak near the magnetic transition, i.e., around T_N . A very similar scenario is also observed for the $U = 12$ case as shown in the same figure. For $U = 6$, the M remains more or less same as we approach T_N from $T \sim 1$, but increases below T_N . For smaller U values, such as $U = 4$, the M values even decrease when the temperature de-

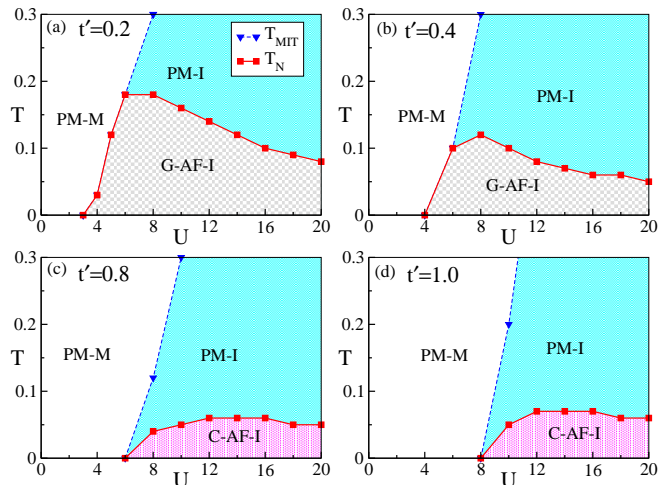


FIG. 2: The U - T phase diagrams at finite t' values: (a) $t' = 0.2$, (b) $t' = 0.4$, (c) $t' = 0.8$, and (d) $t' = 1.0$. As t' increases, the long-range AF order in the low- U regime decreases, favoring the paramagnetic metallic (PM-M) state at low temperatures. At $t' = 0.2$ and $t' = 0.4$, the G-type AF insulating phase vanishes away at lower U values, but remains stable at moderate to high U values. For high t' [$t' = 0.8$ and $t' = 1.0$], the G-type AF insulating phase disappears completely, whereas a C-type AF insulating phase appears for moderate and high U values. Legends are same in panels (a)-(d).

creases from $T \sim 1$ to T_N . The system remains PM-M until T_N for low U values, possibly due to the delocalization of magnetic moments.

IV. $t' \neq 0$ WHILE $t'' = 0$: EFFECT OF THE SECOND-NEAREST-NEIGHBOR HOPPING ON MAGNETOTRANSPORT PROPERTIES

The addition of second-nearest-neighbor hopping (t') introduces frustration by competing with nearest-neighbor hopping t . For $U \leq 3$, the G-type AF insulating phase totally disappears as shown in Fig. 2(a). When $3 < U \leq 6$, the system changes from the PM-M phase to the G-type AF insulating phase as the temperature decreases. For $U \geq 8$, the PM-I phase appears between the PM-M and G-type AF phases, similar to the $t' = 0$ case. It is also important to observe that, in contrast to the non-frustrated situation ($t' = 0$), competitive interactions reduce the transition temperature of the G-type antiferromagnetic phase for all U values when $t' = 0.2$ is added, though only slightly at higher U values. However, the Neel temperature (T_N) exhibits non-monotonic behavior, similar to the $t' = 0$ situation. As t' increases to 0.4, the system stays paramagnetic at the lowest temperature even at $U = 4$ as shown in Fig. 2(b). For $U > 4$, the G-type AF phase is stable at low temperatures. However, the antiferromagnetic transition temperature decreases dramatically for all U values as compared to $t' = 0$ and

$t' = 0.2$ cases. The suppression of T_N due to $t' = 0.4$ is more noticeable for intermediate U values compared to higher U values. These all findings highlight the role that competitive interactions between t and t' play in suppressing the G-type AF insulating phase; that is, a larger t' results in a more noticeable suppression of the G-type AF phase.

As the t' value is increased further, the effect of t' turns into even more dramatic and noticeable. At $t' = 0.8$, G-type AF order is entirely wiped out, resulting in the onset of C-type antiferromagnetic order at higher U values, as shown in Fig. 2(c). The C-type AF phase, which forms when $U > 6$, is insulating, similar to the G-type AF phase. Thus, as the temperature rises for $t' = 0.8$, the system transits from the C-type AF insulating phase to the PM-I phase at higher U values. When $U \leq 6$, long-range magnetic ordering disappears, resulting in the paramagnetic metallic phase, even at low temperatures. The long-range magnetic order does not survive up to $U = 8$ at $t' = 1.0$, as shown in Fig. 2(d). The C-type AF insulating phase appears beyond that U value. So, in the nonperturbative regime, where the on-site Hubbard repulsive strength U is comparable to the electronic bandwidth of the system, introducing significant second-nearest-neighbor hopping (t') shifts the ground state preference from G-type to C-type AF.

We then go into more detail about the magnetic and transport properties, which we utilized to build the U - T phase diagrams shown in Fig. 2. We mainly concentrate on $U = 6$ and $U = 12$ as in Fig. 1 for these analysis. First, we discuss the magnetic and transport properties obtained for $U = 6$. The structure factor calculations demonstrate that the T_N for the G-type AF phase decreases as t' increases, finally vanishing for large t' [see Fig. 3(a)]. In order to determine how the specific heat (C_v) versus temperature for $U = 6$ corresponds to the magnetic transition, it is also shown over a range of t' values in Fig. 3(b). It is clear that the low-temperature peak around $T = 0.1$ corresponds to the respective T_N for $t' = 0.0, 0.2$, and 0.4 . Our calculations also show that the low temperature peak is absent at $t' = 0.8$, which is consistent with the fact that T_N vanishes for this t' .

In addition, we investigated the temperature dependence of resistivity at various t' to determine the relationship between the long-range magnetic ordering and the transport properties. The T_N and the T_{MIT} correspond well for $t' = 0.0, 0.2$, and 0.4 and vanish together at $t' = 0.8$, as shown in Fig. 3(c). Thus, for $t' = 0.8$, the system remains metallic down to low temperatures. In addition, we calculate the density of states (DOS) at $T = 0.01$ to analyze the transport properties, as illustrated in Fig. 3(d). The DOS clearly shows a gap at the Fermi level ($\omega = 0$) for $t' = 0, 0.2$, and 0.4 , indicating an insulating ground state. However, the gap decreases with increasing the value of t' . On the other hand, a finite DOS at the Fermi level for $t' = 0.8$ indicates a metallic ground state. Furthermore, as the temperature decreases from $T \approx 1$, the local magnetic moment (M)

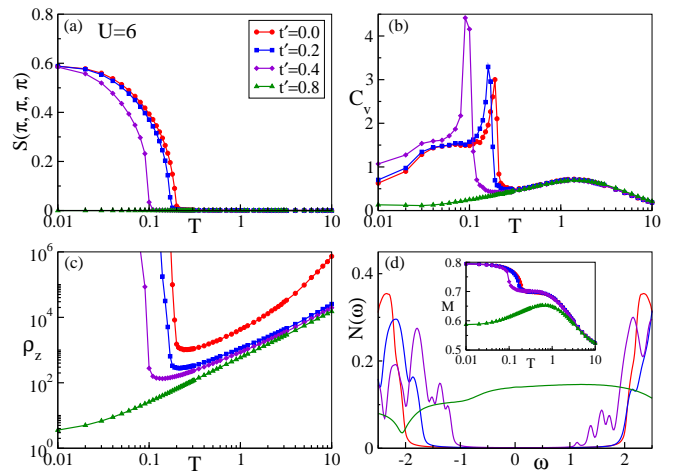


FIG. 3: Physical quantities for $U = 6$ with various t' values: (a) The evolution of structure factor $S(\pi, \pi, \pi)$ with temperature for different t' values. As t' increases, the T_N decreases and eventually disappears for large t' . (b) As t' increases from 0 to 0.4, the low temperature peak in C_v vs. T , indicating the antiferromagnetic transition, shifts to lower temperatures. This peak, however, vanishes at $t' = 0.8$, which is in line with the observation that the magnetic ordering does not exist at this t' . (c) Resistivity ρ_z vs. T plots illustrate that when t' increases, the T_{MIT} falls. At $t' = 0.8$, the system stays in a metallic state even at low temperatures. For every fixed t' value the T_N and T_{MIT} coincide at $U = 6$. (d) The density of states (DOS) at $T = 0.01$ for $t' = 0, 0.2$, and 0.4 displays a gap around the Fermi level ($\omega = 0$), confirming the insulating behavior at low temperatures. As t' increases, the gap decreases, and a finite DOS at Fermi level for $t' = 0.8$ affirms the presence of metallic ground state. The evolution of local moments M with temperature is shown in the inset of (d). For $t' = 0, 0.2$, and 0.4 , M steadily increases below T_N as temperature decreases further. On the other hand, when $t' = 0.8$, where T_N disappears, M continuously decreases below $T \approx 1$, suggesting that the delocalized moment contributes to the enhancement of its metallicity. Legends are same in panels (a)–(d).

in the PM-M phase for $t' = 0.8$ decreases, indicating that a delocalized moment enhances the metallicity, as illustrated in the inset of Fig. 3(d). However, for $t' = 0.2$ and 0.4 , the M stays more or less firm below $T = 1$ and increases below T_N , much like in the $t' = 0$ case, giving rise to insulating state at low temperatures.

Now, we present a variety of physical signatures in Fig. 4 in order to investigate the magnetotransport properties that appear at $U = 12$. The structure factor calculations show that the T_N for the G-type AF phase diminishes as t' grows from 0.0 to 0.4, eventually vanishing for large t' , as illustrated in Fig. 4(a). The C-type AF phase emerges at $t' = 0.8$ and $t' = 1.0$. In Fig. 4(b), we show the temperature-dependent specific heat (C_v) for $U = 12$ at different t' values. For the G-type phase in particular, the systematics of the low-temperature peak of C_v s is in accordance with that of the T_N s demonstrated in Fig. 4(a). Due to competition between three

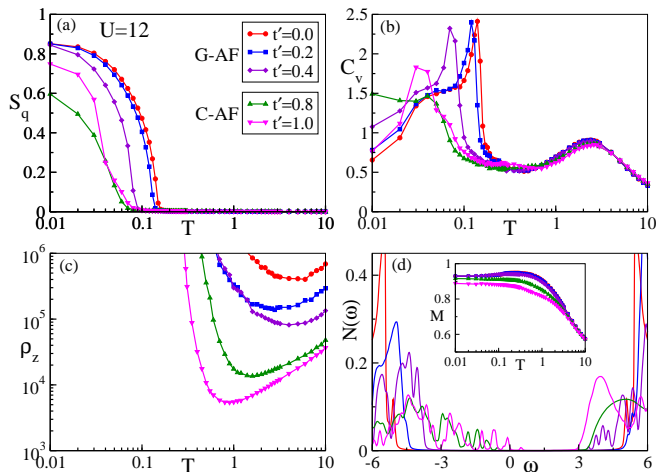


FIG. 4: Physical quantities for $U = 12$ with different t' values: (a) Structure factors for G-type AF ordering are plotted at $t' = 0, 0.2$, and 0.4 , while those for C-type AF ordering are presented at $t' = 0.8$ and 1.0 . When t' ($0, 0.2$, and 0.4) is small, the low temperature magnetic ordering is G-type AF, but T_N decreases as t' increases. On the other hand, the low temperature magnetic order transforms into C-type AF for stronger t' (0.8 and 1) values. (b) The corresponding antiferromagnetic transitions and the low-temperature peak in the C_v vs. temperature curves are coherent. (c) Temperature dependence of resistivity ρ_z exhibits insulating behavior at low temperatures for all t' values. The T_{MIT} decreases as t' increases. (d) Insulating behavior at low temperatures is highlighted by the density of states (DOS) at $T = 0.01$, which displays a gap near the Fermi level ($\omega = 0$). This gap decreases as t' increases. Satellite peaks emerge at the edge of the gap in the C-type AF ordered phase, unlike the G-type AF ordered phase. The temperature evolution of the local moment M is illustrated in the inset of (d). For every t' , M rises with decreasing temperature and reaches saturation at lower temperatures. The saturation value of M at low temperatures decreases gradually with increasing t' . Legends are same in panels (a)–(d).

different types of C-type ordering $S(\pi, \pi, 0)$, $S(0, \pi, \pi)$, and $S(\pi, 0, \pi)$ near the phase transition, the low temperature peak in the C_v is either slightly off the mark or distorted for higher t' values where the C-type phase is stable.

The systematic of T_{MIT} is illustrated in Fig. 4(c). The T_{MIT} decreases as t' increases considerably. As previously mentioned, for $U = 12$, the system stays in highly insulating state at low temperatures. It is also clear that, for any t' , the T_{MIT} is significantly higher than the corresponding T_N values. We show the DOS at $T = 0.01$ in Fig. 4(d) to support our investigation of the transport properties at low temperatures. Our calculations disclose a significant gap at the Fermi level ($\omega = 0$), implying an insulating ground state for all t' values. As temperature decreases from $T \approx 1$, the variation of local magnetic moment (M) at finite t' , where G-type phase remains unaffected, resembles to that of the $t' = 0$ scenario, as illustrated in Fig. 4(d), suggest that the insulating prop-

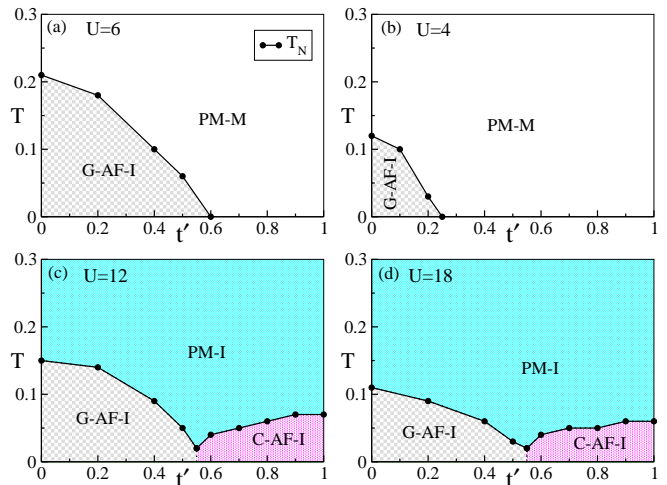


FIG. 5: The t' - T phase diagrams for different U values: (a) $U = 6$, (b) $U = 4$, (c) $U = 12$, and (d) $U = 18$. Compared to $U = 4$, the region over which the G-type AF insulating phase remains stable, is larger for $U = 6$. For smaller U values, the T_N and the T_{MIT} coincide even at finite t' , analogous to the $t' = 0$ scenario, as the system evolves directly from a PM-M phase to a G-type AF insulating phase as the temperature decreases. As t' increases, the T_N values fall until they vanish at $t' = 0.25$ at $U = 6$ ($U = 4$), indicating a low-temperature PM-M phase at higher t' values. Even at finite t' , the T_{MIT} is much greater than T_N for larger U values ($U = 12$ and $U = 18$), due to the formation of a paramagnetic insulating (PM-I) phase between the magnetically ordered insulating phase and the PM-M phase. As the temperature decreases, the PM-I phase evolves to the G-type AF phase for smaller t' (< 0.55). Crucially, the PM-I phase transforms to a C-type AF insulating phase when the temperature decreases for stronger t' (> 0.55). Legends are same in panels (a)–(d).

erty of these systems is preserved. At low temperatures, the saturation value of M decreases as t' increases beyond 0.4 , which reflect that the competing interactions between t and t' somewhat hinder the creation of local moments even at $U = 12$. The drop in T_{MIT} , as illustrated in Fig. 4(c), is in good agreement with the decrease in the saturation value of M at low temperatures with an increase in t' values.

In order to further illustrate the variation in magnetic phases at finite temperatures, we present the t' - T phase diagram for four U values in Fig. 5. The ground state displays a long-range G-type AF insulating phase up to $t' = 0.6$ for $U = 6$, as illustrated in Fig. 5(a). The T_N decreases as t' increases and then expectedly disappears. So, the competitive character of t' prevents magnetic ordering and makes it challenging to maintain long-range G-type AF order at low temperatures, resulting in a decrease in T_N . In other words, beyond a certain t' , competition between t and t' prohibits the system from achieving any long-range magnetic order, retaining a paramagnetic metal (PM-M) as the ground state. Thus, the system remains in a PM-M state due to conflicting in-

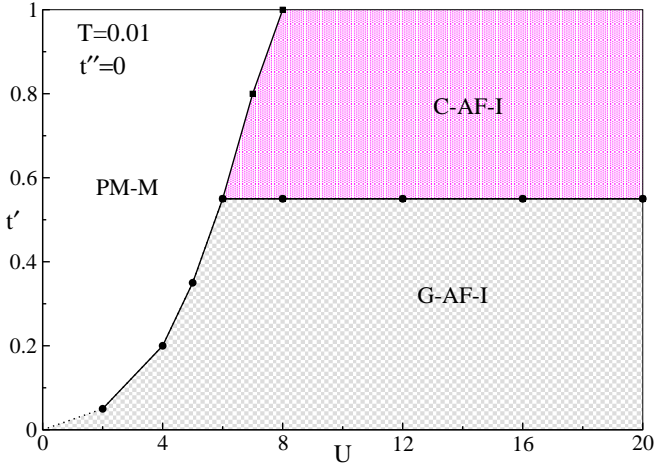


FIG. 6: The U - t' phase diagram at $T = 0.01$: For $U \leq 6$, the G-type AF phase becomes destabilized and a PM-M phase becomes stabilized as t' increases. For $U \geq 8$, the G-type AF insulating phase transitions to the C-type AF insulating phase as t' increases. The value of t' where the G-type to C-type transition occurs, essentially remains unchanged. For $U = 7$, the system transitions from G-type AF insulating to PM-M phase through C-type AF insulating. t'' is set to zero in this plot.

teractions that destabilize the antiferromagnetic order in this regime. At $U = 4$, the G-type AF insulating state only lasts until $t' = 0.25$ [see Fig. 5(b)].

The scenario is significantly different for higher U values. For $U = 12$ and 18 , we present the t' - T phase diagram in Figs. 5(c) and (d), respectively. The ground state remains in the G-type AF insulating state for $t' < 0.55$. The C-type AF insulating phase, in contrast to the PM-M phase in lower U values, becomes the ground state for $t' > 0.55$. The system shows the PM-I phase for all t' values just above the magnetic ordering temperature. Following the system's transition from the G-type AF phase to the C-type AF phase at low temperatures, the T_N of the C-type AF phase initially increases and then remains more or less unchanged with t' . These findings show that whereas weaker Hubbard interactions are more susceptible to competing interactions that disrupt the magnetic ordering, strong interactions (U) preserve a certain magnetic ordering (C-type AF) even at large t' .

To completely demonstrate the impact of t' across different ranges of U values [from weak ($U \ll BW$) to strong ($U \gg BW$)], we provide the ground state U - t' phase diagram in Fig. 6 before we end this section. When U is small, the G-type AF insulating phase is the ground state due to the perseverance of perfect nesting at $t' = 0$. A small amount of t' disturbs this nesting pattern, resulting in a PM metallic phase. So, as t' increases, the G-type AF insulating state changes to a PM-M state at small and modest $U (\leq 6)$ values. At intermediate and strong correlation limits ($U > 6$), the transition from G-type AF insulating to C-type AF insulating state occurs approximately at $t' \approx 0.55$.

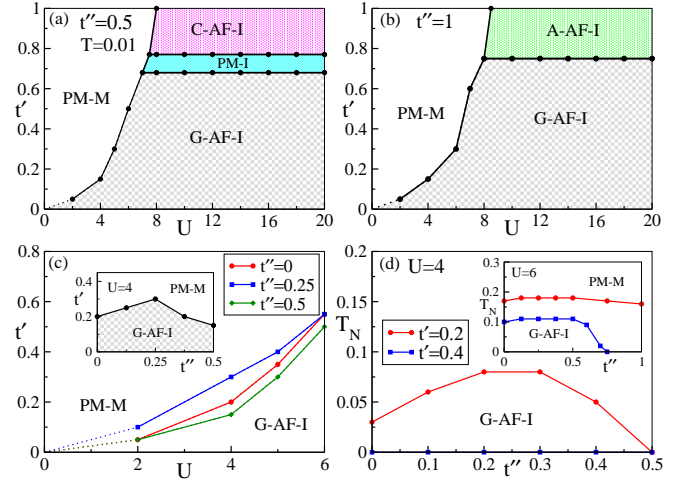


FIG. 7: The effect of t'' : U - t' phase diagrams for (a) $t'' = 0.5$ and (b) $t'' = 1.0$ are displayed to compare to the case when $t'' = 0$. When $t'' = 0.5$, a PM-I phase emerges within a small window of t' ($0.7 \leq t' \leq 0.75$) for $U > 7$, between the G-type and C-type AF phases, as opposed to $t'' = 0$. Otherwise, the phase diagram appears similar to $t'' = 0$. Surprisingly, at $t'' = 1$, the PM-I and C-type AF insulating phases are entirely eliminated, whereas the A-type AF insulating phase emerges for $U > 8$. (c) Comparison of the U - t' phase diagram for $U \leq 6$ for small and modest t'' values ($t'' = 0, 0.25, \text{ and } 0.5$). The G-type AF phase is stable below each curve, whereas the PM-M phase appears above it. As t'' increases from 0 to 0.25, the G-type AF insulating phase expands, indicating a better stability of the G-type AF order. However, the G-type AF phase contracts to lower t' values as t'' increases to 0.5, suggesting decreased stability of the G-type AF order. The inset highlights the non-monotonic nature of t'' for $U = 4$. The stability of the G-type AF order improves from $t'' = 0$ to 0.25, enabling it to persist at higher t' values, but the stability decreases with further rise of t'' , according to the t'' - t' phase diagram in the inset. (d) The t'' - T_N plot for $t' = 0.2$ at $U = 4$ illustrates nonmonotonic behavior of T_N with t'' . Magnetic order is not formed for any t'' when $t' = 0.4$. Inset: The t'' - T_N plot for $U = 6$ indicates a non-monotonic trend of T_N at $t' = 0.4$. When $t' = 0.2$, the T_N remains more or less constant.

V. COMBINED EFFECT OF LONG-RANGE HOPPINGS ($t' \neq 0$ AND $t'' \neq 0$) ON MAGNETOTRANSPORT PROPERTIES

In this section, we investigate various cases in which the third-nearest-neighbor hopping (t'') is finite. We employ the same range of U and t' values that we have used for $t'' = 0$ case in Fig. 6 to study the comprehensive ground state U - t' phase diagram for $t'' = 0.5$ [see Fig. 7(a)]. In contrast to the $t'' = 0$ scenario, a strongly correlated paramagnetic insulating (PM-I) phase separates the G-type AF insulating and C-type AF insulating phases for intermediate to large U values at $t'' = 0.5$, emphasizing the complex interactions between t' and t'' . On the other hand, the PM-I and C-type AF insulating phases totally disappear at $t'' = 1.0$ [see Fig. 7(b)], and

the G-type AF insulating phase switches directly to the A-type AF insulating phase as t' increases. It is also noticeable that the G-type AF insulating phase persists over a substantially greater range of t' than at $t'' = 0.5$, demonstrating the stabilizing influence of higher t'' on the G-type AF phase at higher U values.

To better understand the competition between t , t' , and t'' values, we present the ground state U - t' phase diagram for a smaller range of U values with different t'' values in Fig. 7(c). In this diagram, the G-type AF phase is stable below each of the curve, while the PM-M phase is obtained above it. For small U values, there is clear non-monotonic behavior in terms of stabilization of the G-type AF phase. In order to visualize the situation, we depict the t'' - t' phase diagram in the inset of Fig. 7(c) for $U = 4$. The G-type AF is not stable at $t' > 0.2$ while $t'' = 0$, but becomes stabilized at $t'' = 0.25$. So, a small but finite t'' reduces the negative effect of $t' \neq 0$ on long-range magnetic ordering and helps in strengthening the G-type AF insulating phase at slightly larger t' values. However, further increasing the value of t'' reduces this effect.

At $t' = 0.2$, the T_N also exhibits a non-monotonic trend as t'' increases for $U = 4$ [see Fig. 7(d)]. The G-type AF phase disappears at $t'' = 0.5$. For $t' = 0.4$, the system remains in a PM state, regardless of the t'' values. The inset of the same figure shows the variation of T_N with t'' for $U = 6$. The T_N remains more or less stable with t'' upto $t'' = 1.0$ at $t' = 0.2$ but vanishes beyond $t'' = 0.75$ for $t' = 0.4$.

Next, we examine the t' - T phase diagram for $t'' = 0.25$, 0.5 and 1 in order to better understand the impact of t'' for $U = 12$. For $t'' = 0.5$, as shown in Fig. 8(a), the T_N decreases with increasing t' , similar to the $t'' = 0$ scenario. After $t' = 0.75$, the system shifts to a C-type AF insulating phase, and as t' increases, the T_N for this phase is enhanced slightly. At low temperatures, the transition from G-type to C-type AF phase occurs through the PM-I phase in our calculations. Otherwise, the phase diagram at $t'' = 0.5$ is qualitatively similar to $t'' = 0$ scenario. Additionally, we display the t' - T phase diagram for $t'' = 0.25$ in the inset of Fig. 8(a). In this case, there is essentially no separation between G-type AF and C-type AF phases near their junction similar to $t'' = 0$ case. As t'' increases to 1, the G-type AF insulating phase persists until $t' = 0.75$, as shown in Fig. 8(b). Interestingly, for $t' > 0.75$, a long-range A-type AF insulating phase appears instead of the C-type AF phase, as compared to $t'' = 0.5$ case.

When observing the systematics of the T_N values of the G-type AF phase at small and intermediate t' values, it is clear that the T_N values at $t'' = 1$ are significantly higher than the values observed at $t'' = 0$ or 0.5. This increase in T_N with an increase in t'' values is more apparent from the t'' - T_N plot for $t' = 0, 0.2$, and 0.4 [shown in Fig. 8(c)]. This highlights how the t'' hopping strengthens the G-type AF phase by complementing the t hopping at $U = 12$. In addition, for $t'' = 1$, the Neel temperature of the

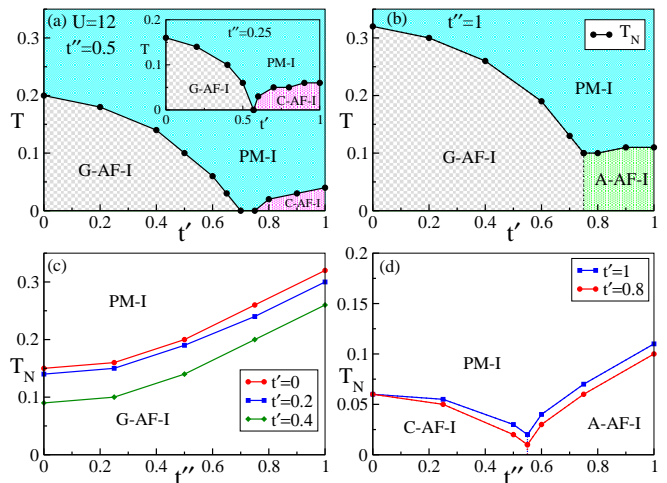


FIG. 8: The t' - T phase diagrams at $U = 12$ are displayed for (a) $t'' = 0.5$ and (b) $t'' = 1$. We use the inset of (a) to illustrate the phase diagram for $t'' = 0.25$. For all three values of t'' , the T_{MIT} is significantly higher than T_N , resulting in the creation of the PM-I phase at temperatures above the magnetically ordered insulating phase. At low to moderate t' , the PM-I phase transitions to the G-type AF insulating phase, while at high t' , it transitions to either the C-type AF insulating phase ($t'' = 0.25$ and 0.5) or the A-type AF insulating phase ($t'' = 1.0$), depending on the value of t'' . The low-temperature G-type AF phase ground state remains stable for $t' < 0.55$, but a C-type AF insulating phase appears for $t' > 0.55$ ($t' > 7$) for $t'' = 0.25$ ($t'' = 0.5$). For $t'' = 0.5$, in the narrow t' window ($0.7 \leq t' \leq 0.75$), the PM-I phase persists down to the lowest accessible temperature, separating the low- t' G-type AF insulating phase from the high- t' C-type insulating phase. At $t'' = 1$ the PM-I phase transitions to the G-type AF insulating phase for $t' < 0.75$, while for $t' > 0.75$, it evolves to the A-type AF insulating phase. (c) As t'' increases, the T_N associated with the G-type AF phase increases for any given t' . But, for a specific t'' , the T_N decreases as t' increases. (d) The T_N decreases as t'' increases in the C-type AF region for $t' = 0.8$ and 1. In contrast, the T_N increases with t'' inside the A-type AF ordered regime. Legends are same in panels (a) and (b).

A-type AF phase is higher than the Neel temperature of the C-type phase that appears in the $t'' = 0$ or $t'' = 0.5$ cases for a given t' value. In Fig. 8(d), we depict the t'' - T_N phase diagram for $t' = 0.8$ and 1.0 in order to demonstrate the systematics of transition temperatures as we traverse from the C-type AF to the A-type AF phase. First, the T_N of the C-type AF phase decreases as t'' grows and then, beyond $t'' = 0.55$, the A-type AF phase appears, and the T_N of A-type AF phase increases with increase in t'' .

Next, using $U = 12$, we demonstrate more details of the magnetic and transport properties with different t'' values for $t' = 1$ in Fig. 9. The structure factor calculations [see Fig. 9(a)] show that the T_N for the C-type AF phase decreases as t'' increases, while the T_N for the A-type AF phase increases as t'' rises from 0.75 to 1. Interestingly, as shown in Fig. 9(b), the metal-insulator tran-

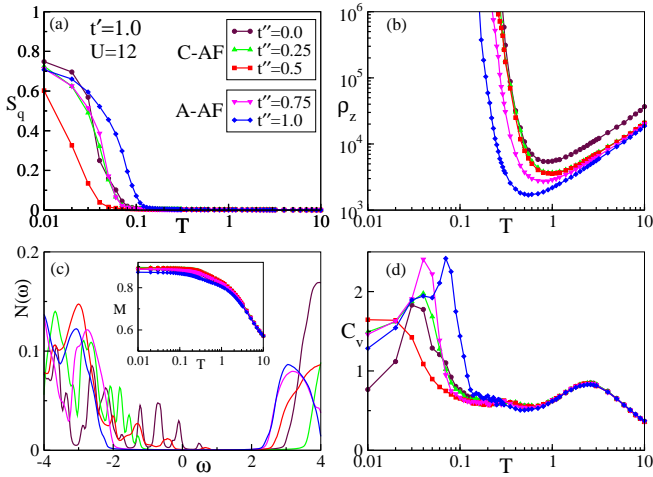


FIG. 9: Physical properties for $U = 12$ at $t' = 1.0$ with different t'' values: (a) Variation of the structure factor $[S(\pi, \pi, 0)/S(\pi, 0, \pi)/S(0, \pi, \pi)]$ for C-type AF order with temperature at $t'' = 0, 0.25$, and 0.5 . The T_N for C-type AF phase decreases as t'' increases from 0 to 0.5. The structural factor for A-type AF order $[S(\pi, 0, 0)/S(0, 0, \pi)/S(0, \pi, 0)]$ vs T demonstrates that when t'' increases from 0.75 to 1, the T_N value increases. (b) Resistivity ρ_z versus T is shown for various t'' . In the C-type AF ordered region, the T_{MIT} slightly increases or remains same as t'' increases from 0 to 0.5, whereas in the A-type ordered region, the T_{MIT} decreases as t'' increases. However, the T_{MIT} is significantly larger than the T_N for all t'' values. (c) At $T = 0.01$, the DOS shows a gap at the Fermi level ($\omega = 0$), confirming the insulating characteristic of all t'' values at low temperatures. In the C-type AF ordered region, increasing t'' do not affect the low temperature saturation value of local moments M , while increasing t'' in the A-type AF ordered region decreases it. (d) The location of the low-temperature peak in specific heat (C_v) varies in accordance with the T_N shown in (a). Although the peak for the C-type AF phase becomes weaker. For more details please see the text. Legends are same in panels (a)–(d).

sition temperature T_{MIT} increases marginally or remains same as t'' increases within the C-type AF ordered region, but it decreases as t'' grows inside the A-type AF phase. However, T_{MIT} is always substantially larger than the corresponding T_N value. To further examine the transport properties, we compute the density of states (DOS) at $T = 0.01$, as shown in Fig. 9(c). The DOS shows a gap at the Fermi level ($\omega = 0$) for all t'' , indicating an insulating ground state. It is crucial to notice that the satellite peaks observed in the gap when $t' = 1$ was introduced [see Fig. 4(c)] are gradually disappeared as one increases t'' . Additionally, inset of Fig. 9(c) shows how the local magnetic moment (M) essentially saturates at low temperatures below $T \approx T_N$, indicating the insulating nature of the system. The observation that T_{MIT} decreases with t'' in the A-type AF ordered region is in good agreement with the saturation value of M at low temperatures, which decreases with increasing t'' . On the other hand, as t'' increases within the C-type AF ordered

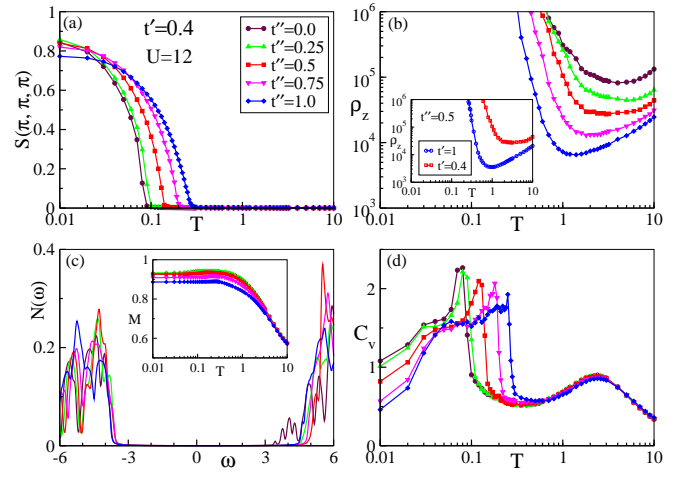


FIG. 10: Physical properties for $U = 12$ at $t' = 0.4$ for various t'' values: (a) The temperature evolution of the structure factor $S(\pi, \pi, \pi)$ corresponding to G-type AF ordering is plotted for $t'' = 0, 0.25, 0.5, 0.75$, and 1 . The T_N increases with increasing t'' . (b) Resistivity ρ_z vs. temperature plots demonstrate that when t'' increases, the T_{MIT} decreases. Furthermore, the T_{MIT} is much greater than T_N for all t'' values. In addition, T_{MIT} values are significantly bigger for the $t' = 0.4$ case than for the $t' = 1$ scenario for any t'' value. Inset: ρ_z vs. T are plotted for $t' = 0.4$ and $t' = 1$ cases using $t'' = 0.5$ to compare the T_{MIT} values. (c) For all t'' , the DOS at $T = 0.01$ shows insulating behavior at low temperatures by displaying a gap around the Fermi level ($\omega = 0$). The temperature variation in local moments M is shown in the inset. At low temperatures, the saturation value of M decreases as t'' increases. (d) As t'' increases, the low-temperature peak in C_v changes to higher temperatures, in line with the G-type AF transition temperature illustrated in (a). Legends are same in panels (a)–(d).

region, the saturation value of M remains more or less same. We additionally exhibit the specific heat (C_v) with temperature for different t'' values in Fig. 9(d) to ascertain whether or not the low temperature peak in the specific heat and the T_N relate with one another. In fact, the trend of the temperature at which the low-temperature peak of C_v is observed for all t'' is roughly connected to the T_N systematics in both A-type and C-type AFs. The low-temperature peak of C_v broadens around switching points of the magnetic phases, as previously mentioned.

We also present the magnetotransport properties for $t' = 0.4$ for comparison in Fig. 10. The structure factor calculations show that the T_N for the G-type AF phase increases with increasing t'' , as shown in Fig. 10(a). This is in contrast to the $t' = 1$ scenario, in which the system initially stays in the C-type AF phase (i.e., for small and intermediate t'' values) before transitioning to the A-type AF phase. In Fig. 10(b), it is clear that when t'' increases, the T_{MIT} decreases. Similar to the $t' = 1$ scenario, T_{MIT} s are significantly larger than T_N s. In addition, we calculate the DOS at $T = 0.01$ in Fig. 10(c). For every t'' , the DOS shows a distinct large gap at the

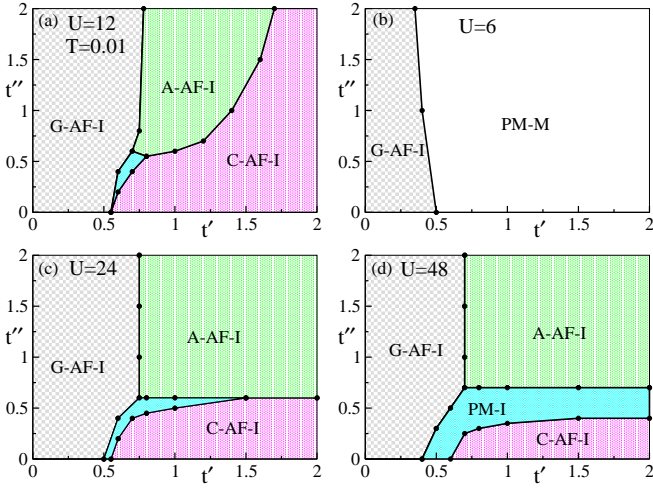


FIG. 11: t' - t'' phase diagrams for different U values at $T = 0.01$: (a) $U = 12$, (b) $U = 6$, (c) $U = 24$, and (d) $U = 48$. When $t'' = 0$, the system directly transitions from the G-type AF insulating phase to a C-type AF insulating phase with increasing t' for $U = 12$. As t'' increases, a PM-I phase separates the G-type and C-type AF insulating phases. When $t'' > 0.6$, the PM-I phase disappears and the G-type AF insulating phase changes directly to the A-type AF insulating phase. As t' value increases further, the system eventually transitions from the A-type AF insulating phase to the C-type AF insulating phase. However, the C-type AF-I phase that occurs when large t' and t'' values are coupled at $U = 12$ is not observed for $U = 24$ or $U = 48$. As U grows from 12 to 24 to 48, the correlated PM-I phase at the intersection of three AF phases expands, primarily suppressing the C-type AF-I phase. For $U = 6$, the phase diagram in (b) demonstrates that only one kind of long-range magnetic phase persists. Beyond a reasonable $t' \sim 0.5$, long-range magnetic ordering breaks down for all t'' values, stabilizing the PM-M phase.

Fermi level ($\omega = 0$), in contrast to the $t' = 1$ scenario. It is also noticeable that the T_{MIT} values are significantly bigger for the $t' = 0.4$ case than for the $t' = 1$ scenario for any t'' value [see inset of Fig. 10(c) for $t'' = 0.5$], which is consistent with the large gap. Additionally, the M vs. temperature curve in the inset of Fig. 10(c) reflects the systematics of T_{MIT} . The saturation magnetization at low temperatures is significantly higher than that of the $t' = 1$ cases shown in the inset of Fig. 9(c). Furthermore, for $t' = 0.4$, the saturation magnetization at low temperatures decreases with increasing t'' , which is consistent with a decrease in T_{MIT} shown in Fig. 10(b). We additionally demonstrate the temperature-dependent specific heat (C_v) for different t'' values in Fig. 10(d) for completeness. The T_N values correspond to the temperature where low-temperature peak of C_v occur for all t'' values. Increasing t'' shifts the low-temperature peak of the C_v to higher temperatures, analogous to the enhancement of T_N as shown in Fig. 10(a).

Now we demonstrate the t' - t'' phase diagrams at low temperature ($T = 0.01$) for different on-site repulsion strengths U in Fig. 11 to comprehend the fine aspects

of magnetotransport properties. For $U = 12$, the G-type AF phase is stable for small and moderate t' values, as shown in Fig. 11(a). If one observes closely, the G-type AF's disappearance shifts toward larger t' values as t'' increases for $t'' \lesssim 0.75$. This happens as a result of t'' maintaining the stability of the G-type AF phase by supporting t , the nearest-neighbor hopping. On the other hand, even in this small and intermediate t'' ($\lesssim 0.55$) range, the C-type AF becomes stabilized at higher t' values. Significantly, when t' increases, the system evolves from the G-type AF phase to the C-type AF phase via a paramagnetic insulating (PM-I) phase in intermediate t'' regime. At higher t'' values, i.e., $t'' \gtrsim 0.55$ the system switches directly to the A-type AF phase from the G-type AF phase as t' increases. At very large t' values, however, the system eventually converts to the C-type AF phase. Thus, our whole phase diagram illustrates how multiple magnetic phases in a half-filled system compete with one another due to a variety of conflicting interactions for $U = 12$. Importantly, the PM-I phase that appears near the junction of three different types of magnetic insulating phases persists into the strong-coupling limit. The lack of magnetic order down to $T = 0.01$ characterizes this region. So, the occurrence can be attributed to a quantum-disordered regime of the local moments. Interestingly, the PM-I phase emerges in intermediate t' and t'' values, disrupting the balance between the AF phases at the phase boundaries. Therefore, the additional fluctuation processes provided by t'' successfully destroy long-range order and preserve the insulating character, even though the competition between t and t' alone is insufficient to accomplish this. However, its presence is restricted to a small region. The formation of the PM-I state can be traced to quantum fluctuations in strongly correlated materials³⁹.

We also illustrate the t' - t'' phase diagram for $U = 6$ in Fig. 11(b). The phase diagram shows only one long-range magnetic phase: the G-type AF phase. Long-range magnetic order breakdown occurs beyond a moderate t' value (e.g., $t' \sim 0.5$ for $t'' = 0$), stabilizing the low- U PM-M phase. Increasing t'' does not dramatically affect the boundary between the G-type AF insulating and PM-M ground states, which remains mostly unaltered.

The competition between the various phases shown for $U = 12$ is maintained when the U value is increased to 24 as shown in Fig. 11(c). The C-type AF phase, which was stable for large t' and t'' values at $U = 12$, is no longer stable at $U = 24$. However, the A-type AF phase is extended to that regime. In this case, a PM-I phase also emerges between the junction of G-, C-, and A-type AF phases. This PM-I phase separates the C-type and A-type AF phases as the t'' value is increased for a fixed t' value near $t' = 1$. Overall, the area covered by the PM-I phase for $U = 24$ is larger than for $U = 12$.

In contrast to $U = 12$, it is important to note that the PM-I phase has apparently stabilized for a range of t' , albeit small, even if $t'' = 0$. The range across which the PM-I phase is stabilized at $t'' = 0$ gets broader when the

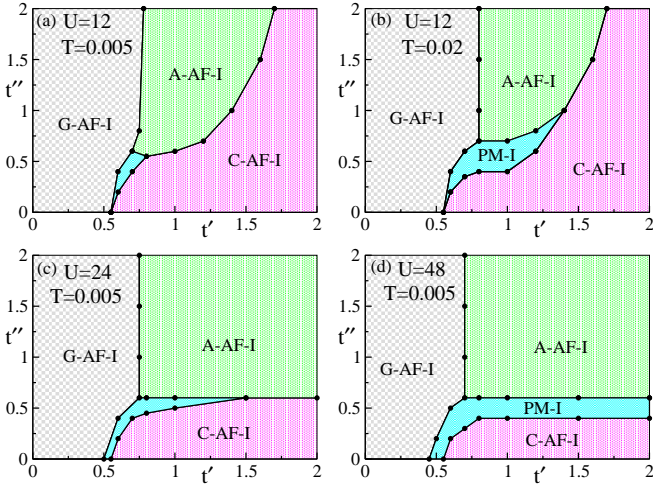


FIG. 12: t' - t'' phase diagrams for various combinations of U and T values: (a) For $U = 12$ at $T = 0.005$; (b) for $U = 12$ at $T = 0.02$; (c) for $U = 24$ at $T = 0.005$; (d) for $U = 48$ at $T = 0.005$. The phase diagram for $U = 12$ at $T = 0.005$ is very similar to the phase diagram at $T = 0.01$ illustrated in Fig. 11(a). In contrast to $T = 0.01$ and 0.005 , the PM-I region is amplified at $T = 0.02$. The phase diagram at $T = 0.005$ remains unchanged from the one at $T = 0.01$ in Fig. 11(c), when $U = 24$. On the other hand, the PM-I phase region for $U = 48$ at $T = 0.005$ is somewhat smaller than the PM-I phase at $T = 0.01$ in Fig. 11(c).

U value is raised to 48 [see Fig. 11(d)]. Increasing U values also enriches the PM-I region at $U = 48$ while reducing the C-type AF phase. Otherwise, the t' - t'' phase diagram looks similar to that of $U = 24$ [compare Fig. 11(d) and (c)].

Overall, as shown in Fig. 11, our calculations reveal that strong electron correlations and long-range magnetic interactions can combine to produce a variety of magnetic phases at low temperatures. Interestingly, low temperatures, long-range interactions, and quantum processes can all combine to produce novel paramagnetic insulating phases that go against expectations. Is the PM-I phase that we observed at $T = 0.01$ stable at even lower temperatures? In order to answer this, we plot the t' - t'' magnetic phase diagram for $U = 12$ at $T = 0.005$ and $T = 0.02$ in Fig. 12(a) and Fig. 12(b), respectively. The PM-I region captured at $T = 0.01$ is evidently unaltered at $T = 0.005$, but it enlarges for $T = 0.02$. This demonstrates that when the temperature decreases, the PM-I phase remains remarkably stable. The stability of the PM-I phase at lower temperatures is also demonstrated for $U = 24$ and $U = 48$ in the Figs. 12(c) and (d), respectively.

When a PM-I phase occurs at low temperatures in presence of long-range interactions it raises the possibility of a spin liquid state. In other words, the combination of long-range interactions and paramagnetic insulation may produce ideal conditions for the formation of spin liquid states in strongly correlated systems. Overall, a PM-I

phase with long-range interactions may support a spin liquid state, but this is not guaranteed. Also, stabilizing spin-liquid states in three dimensions is more challenging than in two dimensions due to weakening of quantum fluctuations as dimensionality increases. So, the identification of a potential host for spin-liquid phase in a three-dimensional Hubbard model with long-range interactions is also interesting.

Similar non-magnetic insulating regions in the phase diagram have also been found in earlier studies^{74,84-89} employing various methods such as the variational cluster approach³⁹. These results further suggest the possibility that this system might host three-dimensional quantum spin liquid phases. Given the long-range interactions in a strongly correlated electron system, our findings are consistent with previous studies that suggested possibility of a spin-liquid phase. However, we agree that advanced quantum many-body techniques, such as Density Matrix Renormalization Group (DMRG) or Quantum Monte Carlo (QMC), can provide a more accurate description of the ground state and low-energy excitations in the paramagnetic insulating region, leading to a better understanding of their nature.

VI. CONCLUSION

Using the s-MC approach, we examined the effects of long-range hoppings (t' and t'') beyond the nearest-neighbor hopping t on the electronic and magnetic properties of the half-filled Hubbard model on a cubic lattice. We performed an extensive study of the processes in which long-range hopping and the degree of electron-electron interaction combine to drive different magnetic phase transitions at low temperatures. The finite-temperature evolution of the G-, A-, and C-type AF phases as well as the underlying metal-insulator transitions were investigated thoroughly. In non-perturbative limit, where electron-electron interaction $U \sim$ bandwidth, the T_{MIT} is much larger than the T_N , resulting in a PM-I phase at temperatures higher than T_N . Interestingly, a novel PM-I phase is created by the combined influence of long-range interaction and quantum processes at very low temperatures. This PM-I phase emerges in intermediate t' and t'' values and lies at the intersection of three distinct AF insulating phases. Our calculations clearly demonstrate that the additional fluctuating processes, introduced by t'' , provides actually aid in triggering the collapse of long range order while maintaining the insulating nature of the system at low temperatures, even though the competition between t and t' is generally insufficient to accomplish this at $U \sim$ bandwidth. This PM-I phase percolate to $t'' = 0$ for $U \gg$ bandwidth limit. Does this PM-I phase host a 3D spin-liquid phase? Validating the spin-liquid phase requires detailed theoretical computations of spin-spin interactions and excitations, which are beyond the scope of this paper. We leave this as a topic for future studies. Overall, our findings

are significant because they shed light on the complex behavior of magnetic systems in the presence of long-range interactions in correlated electron systems, which has implications for exploration and designing of novel materials with exotic electronic and magnetic properties. The finding of a potential candidate for spin-liquid phase in a three-dimensional Hubbard model with long-range interactions is particularly noteworthy. The theoretical insights from this work may provide useful direction for experiments aimed at creating novel materials with particular magnetic properties or those that could potentially host a three-dimensional spin-liquid state.

Acknowledgment

We acknowledge use of the Meghnad2019 computer cluster at SINP.

Appendix A: Effective spin-fermion Hamiltonian

To initiate the semiclassical Monte-Carlo (s-MC) technique, we begin by dissociating the interaction term in Eq. 1 through the conventional Hubbard–Stratonovich (HS) transformation, introducing auxiliary fields. This involves expressing the interaction term at each lattice site in a decouple manner as demonstrated below,

$$n_{i\uparrow}n_{i\downarrow} = \frac{1}{4}n_i^2 - S_{iz}^2 = \frac{1}{4}n_i^2 - (\mathbf{S}_i \cdot \hat{\Omega}_i)^2. \quad (\text{A1})$$

In this context, the spin operator at site i is defined as $\mathbf{S}_i = \frac{1}{2} \sum_{\alpha\beta} c_{i\alpha}^\dagger \sigma_{\alpha\beta} c_{i\beta}$, where $\hbar = 1$. Here, $\sigma = (\sigma_x, \sigma_y, \sigma_z)$ represents the Pauli matrices. Additionally, $\hat{\Omega}_i$ denotes an arbitrary unit vector at site i . We leverage the rotational invariance of S_{iz}^2 , thus, $(\mathbf{S}_i \cdot \hat{\Omega}_i)^2 = S_{ix}^2 = S_{iy}^2 = S_{iz}^2$.

The partition function for the Hamiltonian is given by $Z = \text{Tr}[\exp(-\beta H)]$, where H corresponds to the Hamiltonian stated in Eq. 1. The trace is performed over the occupation number basis, encompassing all particle numbers and site occupations. Here, $\beta = 1/T$ represents the inverse temperature, with the Boltzmann constant k_B set to 1. The interval $[0, \beta]$ is segmented into M equidistant slices, each separated by an interval $\Delta\tau$, where $\beta = M\Delta\tau$. Utilizing Suzuki-Trotter decomposition, as $\Delta\tau$ tends towards zero for very large value of M , we express $\exp[-\beta(H_0 + H_I)]$ approximately as $[\exp(-\Delta\tau H_0) \exp(-\Delta\tau H_I)]^M$ up to the first order in $\Delta\tau$.

Utilizing Eq. A1, for a given time slice ‘ l ’, the interacting part of the partition function can be demonstrated

to be proportional to

$$\int d\phi_i(l) d\Delta_i(l) d^2\Omega_i(l) \exp\left(-\Delta\tau \left\{ \sum_i \left[\frac{\phi_i(l)^2}{U} + i\phi_i(l)n_i + \frac{\Delta_i(l)^2}{U} - 2\Delta_i(l)\hat{\Omega}_i(l) \cdot \mathbf{S}_i \right] \right\}\right), \quad (\text{A2})$$

where, $\phi_i(l)$ represents the auxiliary field associated with charge density, $\Delta_i(l)$ stands for the auxiliary field linked with spin density, and $\hat{\Omega}_i(l)$ is an arbitrary unit vector. Furthermore, we define a new vector auxiliary field $\mathbf{m}_i(l) = \Delta_i(l)\hat{\Omega}_i(l)$. $\phi_i(l)$ couples to the local charge density operator, while $\mathbf{m}_i(l)$ couples to the local spin operator. Consequently, the full partition function is proportional to

$$\text{Tr} \prod_{l=M}^1 \int d\phi_i(l) d^3\mathbf{m}_i(l) \exp\left(-\Delta\tau \left\{ H_0 + \sum_i \left[\frac{\phi_i(l)^2}{U} + i\phi_i(l)n_i + \frac{\mathbf{m}_i(l)^2}{U} - 2\mathbf{m}_i(l) \cdot \mathbf{S}_i \right] \right\}\right), \quad (\text{A3})$$

where, the integrals are taken over $\{\phi_i(l), \mathbf{m}_i(l)\}$. The product order for the slices ranging from $l = M$ to $l = 1$ implies time-ordered products over time slices, with earlier times positioned to the right. It is important to note that at this stage, the partition function is exact, showcasing SU(2) symmetry, and the $\{\phi_i(l), \mathbf{m}_i(l)\}$ fields fluctuate in both space and imaginary time. Now we proceed by making the following approximations: (i) retaining solely the spatial dependence of the auxiliary field variables by dropping the τ dependence of auxiliary field, and (ii) employing a saddle point value for the auxiliary fields, $i\phi_i = \frac{U}{2}(n_i)$. Then, with the redefinition $\mathbf{m}_i \rightarrow \frac{U}{2}\mathbf{m}_i$, the above approximation facilitates the derivation of the effective spin-fermion type Hamiltonian H_{eff} as stated in Eq. 2, where fermions couple to classical auxiliary fields $\{\mathbf{m}_i(l)\}$.

Appendix B: Observable definitions

To determine the ground state magnetic ordering, we calculate the quantum correlations $S(\mathbf{q})$, defined as,

$$S(\mathbf{q}) = \frac{1}{(L^3)^2} \sum_{kl} \langle \mathbf{s}_k \cdot \mathbf{s}_l \rangle \exp[-i\mathbf{q} \cdot (\mathbf{r}_k - \mathbf{r}_l)]. \quad (\text{B1})$$

Here, the angular brackets imply quantum and thermal averaging at all individual sites. The indices $\{k, l\}$ sum over all L^3 sites. The wave vector \mathbf{q} characterizes various magnetic orderings: $\mathbf{q} = (\pi, \pi, \pi)$ denotes G-type AF order, $\mathbf{q} = (0, \pi, \pi), (\pi, 0, \pi), (\pi, \pi, 0)$ signifies C-type AF order, and $\mathbf{q} = (0, 0, \pi), (\pi, 0, 0), (\pi, 0, 0)$ stands for A-type AF order.

The average local moment, defined as the square of the quantum magnetization, is expressed as,

$$M = \langle (n_\uparrow - n_\downarrow)^2 \rangle = \langle n \rangle - 2 \langle n_\uparrow n_\downarrow \rangle. \quad (\text{B2})$$

Here $\langle n \rangle = \langle n_\uparrow + n_\downarrow \rangle$ represents the average occupation number of the system. In the limit $U \rightarrow \infty$ at any finite temperature, the double occupation $\langle n_\uparrow n_\downarrow \rangle \rightarrow 0$. At half-filling, where $\langle n \rangle = 1$, this leads to $M \rightarrow 1$. For the uncorrelated case ($U = 0$) or at very high temperatures ($T \rightarrow \infty$) for finite U , the double occupation satisfies $\langle n_\uparrow n_\downarrow \rangle \rightarrow \langle n_\uparrow \rangle \langle n_\downarrow \rangle$. At half filling which implies $\langle n_\uparrow \rangle = \langle n_\downarrow \rangle = 0.5 \Rightarrow M = 0.5$. Thus, for any real system at half-filling, the local moment M lies between 0.5 and 1.

The specific heat of the system is calculated by differentiating the total energy with respect to temperature (by employing the central difference formula for the derivative),

$$C_v(U, T) = \frac{dE(U, T)}{dT}. \quad (\text{B3})$$

To study transport properties, we calculate the density of states (DOS) and resistivity. The DOS is defined as

$$N(\omega) = \sum_{i=1}^{2L^3} \delta(\omega - \epsilon_i), \quad (\text{B4})$$

where ϵ_i are the single-particle eigenvalues of the effective Hamiltonian [2](#). We use a Lorentzian representation of the delta function with a broadening of $\sim BW/(2L^3)$ to evaluate the DOS, where BW represents non-interacting bandwidth and L^3 is the total number of lattice sites.

The resistivity is determined by inverting the d.c. limit of the optical conductivity, which is obtained using the

Kubo-Greenwood formula^{42,90,91}. The optical conductivity is defined as,

$$\sigma(\omega) = \frac{A}{L^3} \sum_{\alpha, \beta} (n_\alpha - n_\beta) \frac{|f_{\alpha\beta}|^2}{\epsilon_\beta - \epsilon_\alpha} \delta[\omega - (\epsilon_\beta - \epsilon_\alpha)], \quad (\text{B5})$$

with $A = \frac{\pi e^2}{\hbar a_0}$ (a_0 is the lattice parameter). The $f_{\alpha\beta} = \langle \psi_\alpha | \hat{j}_z | \psi_\beta \rangle$ are the matrix elements for the current operator $\hat{j}_z = ia_0 \sum_{i,\sigma} [t(c_{i,\sigma}^\dagger c_{i+a_0\hat{z},\sigma} - h.c.) + t'(c_{i,\sigma}^\dagger c_{i+a_0\hat{z}+a_0\hat{x},\sigma} - h.c.) + t''(c_{i,\sigma}^\dagger c_{i+a_0\hat{z}+a_0\hat{y},\sigma} - h.c.) + t'''(c_{i,\sigma}^\dagger c_{i+a_0\hat{x}+a_0\hat{y}+a_0\hat{z},\sigma} - h.c.)]$. Here, ϵ_α and $|\psi_\alpha\rangle$ are the eigenvalues and associated eigenvectors of the effective Hamiltonian [2](#), respectively, and $n_\alpha = f(\mu - \epsilon_\alpha)$ is the Fermi function. The average d.c. conductivity σ_{dc} is calculated by integrating over a small frequency window $\Delta\omega$,

$$\sigma_{dc} = (\Delta\omega)^{-1} \int_0^{\Delta\omega} \sigma(\omega) d\omega. \quad (\text{B6})$$

$\Delta\omega$ is set four to five times larger than the system's mean finite size gap (average eigen value separation), which is calculated as the ratio of bandwidth BW to total number of eigen values.

* Electronic address: kalpataru.pradhan@saha.ac.in

¹ C. Lacroix, P. Mendels, and F. Mila (eds.), *Introduction to Frustrated Magnetism* (Springer, Berlin, Heidelberg, 2011).

² E. Dagotto and Y. Tokura, *Multifunctional Oxide Heterostructures*, (Oxford University Press, 2012).

³ S. Sachdev, *Quantum Phases of Matter* (Cambridge University Press, 2023).

⁴ F. Herman, Theoretical Investigation of the Electronic Energy Band Structure of Solids, *Rev. Mod. Phys.* **30**, 102 (1958).

⁵ P. W. Anderson, The Resonating Valence Bond State in La_2CuO_4 and Superconductivity, *Science* **235**, 1196 (1987).

⁶ M. R. Norman, High-temperature superconductivity in the iron pnictides, *APS Physics* **1**, 21 (2008).

⁷ T. J. Liu, J. Hu, B. Qian, D. Fobes, Z. Q. Mao, W. Bao, M. Reehuis, S. A. J. Kimber, K. Prokeš, S. Matas, D. N. Argyriou, A. Hiess, A. Rotaru, H. Pham, L. Spinu, Y. Qiu, V. Thampy, A. T. Savici, J. A. Rodriguez, and C. Broholm, From $(\pi, 0)$ magnetic order to superconductivity with (π, π) magnetic resonance in $\text{Fe}_{1.02}\text{Te}_{1-x}\text{Se}_x$, *Nat. Mater.* **9**, 718 (2010).

⁸ B. Keimer, S. A. Kivelson, M. R. Norman, S. Uchida, and J. Zaanen, From quantum matter to high-temperature superconductivity in copper oxides, *Nature* **518**, 179 (2015).

⁹ C. N. R. Rao and A. K. Cheetham, Giant magnetoresis-

tance in transition metal oxides, *Science* **272**, 369 (1996).

¹⁰ K. H. Jergen Buschow, R. W. Cahn, M. C. Flemings, B. Ilschner, E. J. Kramer, S. Mahajan, and P. Veysiere, *Encyclopedia of Materials: Science and Technology*, (Elsevier, Oxford, 2001), pp. 3521–3531.

¹¹ P. Fazekas and P. W. Anderson, On the ground state properties of the anisotropic triangular antiferromagnet, *Philos. Mag.* **30**, 423 (1974).

¹² S. Sachdev, Quantum magnetism and criticality, *Nat. Phys.* **4**, 173 (2008).

¹³ L. Balents, Spin liquids in frustrated magnets, *Nature* **464**, 199 (2010).

¹⁴ S. Lee, R. K. Kaul, and L. Balents, Interplay of quantum criticality and geometric frustration in columbite, *Nat. Phys.* **6**, 702 (2010).

¹⁵ W. Witczak-Krempa, G. Chen, Y. B. Kim, and L. Balents, Correlated Quantum Phenomena in the Strong Spin-Orbit Regime, *Annu. Rev. Condens. Matter Phys.* **5**, 57 (2014).

¹⁶ A. Soumyanarayanan, N. Reyren, A. Fert, and C. Panagopoulos, Emergent phenomena induced by spin-orbit coupling at surfaces and interfaces, *Nature* **539**, 509 (2016).

¹⁷ A. Georges, G. Kotliar, W. Krauth, and M. J. Rozenberg, Dynamical mean-field theory of strongly correlated fermion systems and the limit of infinite dimensions, *Rev. Mod. Phys.* **68**, 13 (1996).

¹⁸ G. Rohringer, A. Toschi, A. Katanin, and K. Held, Crit-

- ical properties of the half-filled Hubbard model in three dimensions, *Phys. Rev. Lett.* **107**, 256402 (2011).
- 19 T. Sato and H. Tsunetsugu, Cluster dynamical mean field theory study of antiferromagnetic transition in the square-lattice Hubbard model: Optical conductivity and electronic structure, *Phys. Rev. B* **94**, 085110 (2016).
 - 20 L. Fratino, P. Semon, M. Charlebois, G. Sordi, and A.-M. S. Tremblay, Signatures of the Mott transition in the antiferromagnetic state of the two-dimensional Hubbard model, *Phys. Rev. B* **95**, 235109 (2017).
 - 21 R. Blankenbecler, D. J. Scalapino, and R. L. Sugar, Monte Carlo calculations of coupled boson-fermion systems. I, *Phys. Rev. D* **24**, 2278 (1981).
 - 22 R. Staudt, M. Dzierzawa, and A. Muramatsu, Phase diagram of the three-dimensional Hubbard model at half filling, *Eur. Phys. J. B* **17**, 411 (2000).
 - 23 W. M. C. Foulkes, L. Mitras, R. J. Needs, and G. Rajagopal, Quantum Monte Carlo simulations of solids, *Rev. Mod. Phys.* **73**, 33–83 (2001).
 - 24 D. Senechal, A. M. Tremblay, and C. Bourbonnais, *Theoretical Methods for Strongly Correlated Electrons*, (Springer, New York, 2004), pp. 39–74.
 - 25 P. Corboz and F. Mila, Crystals of bound states in the magnetization plateaus of the Shastry-Sutherland model, *Phys. Rev. Lett.* **112**, 147203 (2014).
 - 26 P. C. G. Vlaar and P. Corboz, Simulation of three-dimensional quantum systems with projected entangled-pair states, *Phys. Rev. B* **103**, 205137 (2021).
 - 27 P. C. G. Vlaar and P. Corboz, Efficient tensor network algorithm for layered systems, *Phys. Rev. Lett.* **130**, 130601 (2023).
 - 28 M. C. Banuls, Tensor Network Algorithms: A Route Map, *Annu. Rev. Condens. Matter Phys.* **14**, 173 (2023).
 - 29 A. L. Cavalieri, N. Müller, Th. Uphues, V. S. Yakovlev, A. Baltuska, B. Horvath, B. Schmidt, L. Blumel, R. Holzwarth, S. Hendel, M. Drescher, U. Kleineberg, P. M. Echenique, R. Kienberger, F. Krausz, and U. Heinzmann, Attosecond spectroscopy in condensed matter, *Nature* **449**, 1029 (2007).
 - 30 V. N. Valmispild, E. Gorelov, M. Eckstein, A. I. Lichtenstein, H. Aoki, M. I. Katsnelson, M. Yu. Ivanov, and O. Smirnova, Sub-cycle multidimensional spectroscopy of strongly correlated materials, *Nat. Photonics* **18**, 432 (2024).
 - 31 R. Wiesendanger, Spin mapping at the nanoscale and atomic scale, *Rev. Mod. Phys.* **81**, 1495 (2009).
 - 32 F. Eickhoff, E. Kolodzeiski, T. Esat, N. Fournier, C. Wagner, T. Deilmann, R. Temirov, M. Rohlfing, F. S. Tautz, and F. B. Anders, Inelastic electron tunneling spectroscopy for probing strongly correlated many-body systems by scanning tunneling microscopy, *Phys. Rev. B* **101**, 125405 (2020).
 - 33 C. Gross and I. Bloch, Quantum simulations with ultracold atoms in optical lattices, *Science* **357**, 995 (2017).
 - 34 F. Schafer, T. Fukuhara, S. Sugawa, Y. Takasu, and Y. Takahashi, Tools for quantum simulation with ultracold atoms in optical lattices, *Nat. Rev. Phys.* **2**, 411 (2020).
 - 35 T. Langen, G. Valtolina, D. Wang, and J. Ye, Quantum state manipulation and cooling of ultracold molecules, *Nature Physics* **20**, 702 (2024).
 - 36 R. K. Goyal, S. Maharaj, P. Kumar, and M. Chandrasekhar, Exploring quantum materials and applications: a review, *J. Mater. Sci. Mater. Eng.* **20**, 4 (2025).
 - 37 M. Raczkowski, A. M. Oleś, and R. Frésard, Half-filled stripes in the t - t' - U Hubbard model, *phys. stat. sol. (b)* **243**, 128 (2006).
 - 38 E. Langmann and M. Wallin, Mean Field Magnetic Phase Diagrams for the Two Dimensional t - t' - U Hubbard Model, *J. Stat. Phys.* **127**, 825 (2007).
 - 39 M. Laubach, D. G. Joshi, J. Reuther, R. Thomale, M. Vojta, and S. Rachel, Quantum disordered insulating phase in the frustrated cubic-lattice Hubbard model, *Phys. Rev. B* **93**, 041106 (2016).
 - 40 L. Fratino, M. Charlebois, P. Semon, G. Sordi, and A. M. S. Tremblay, Effects of interaction strength, doping, and frustration on the antiferromagnetic phase of the two-dimensional Hubbard model, *Phys. Rev. B* **96**, 241109 (2017).
 - 41 G. Jana and A. Mukherjee, Frustration effects at finite temperature in the half-filled Hubbard model, *J. Phys.: Condens. Matter* **32**, 365602 (2020).
 - 42 S. Chakraborty, A. Mukherjee, and K. Pradhan, Antiferromagnetism beyond the classical percolation threshold in the diluted half-filled one-band Hubbard model in three dimensions, *Phys. Rev. B* **106**, 075146 (2022).
 - 43 C. W. Liu, S. Liu, Y. J. Kao, A. L. Chernyshev, and A. W. Sandvik, Impurity-Induced Frustration in Correlated Oxides, *Phys. Rev. Lett.* **102**, 167201 (2009).
 - 44 J. Y. P. Delannoy, M. J. P. Gingras, P. C. W. Holdsworth, and A. M. S. Tremblay, Low-energy theory of the t - t' - t'' - U Hubbard model at half-filling: Interaction strengths in cuprate superconductors and an effective spin-only description of La_2CuO_4 , *Phys. Rev. B* **79**, 235130 (2009).
 - 45 C. Krellner, N. Caroca-Canales, A. Jesche, H. Rosner, A. Ormeci, and C. Geibel, Magnetic and structural transitions in layered iron arsenide systems: AFe_2As_2 versus RFeAsO , *Phys. Rev. B* **78**, 100504 (2008).
 - 46 C. de la Cruz, Q. Huang, J. W. Lynn, J. Li, W. Ratcliff II, J. L. Zarestky, H. A. Mook, G. F. Chen, J. L. Luo, N. L. Wang, and P. Dai, Magnetic order close to superconductivity in the iron-based layered $\text{LaO}_{1-x}\text{F}_x\text{FeAs}$ systems, *Nature* **453**, 899 (2008).
 - 47 D. Jaksch and P. Zoller, The cold atom Hubbard toolbox, *Ann. Phys.* **315**, 52 (2005).
 - 48 R. A. Hart, P. M. Duarte, T.-L. Yang, X. Liu, T. Paiva, E. Khatami, R. T. Scalettar, N. Trivedi, D. A. Huse, and R. G. Hulet, Observation of antiferromagnetic correlations in the Hubbard model with ultracold atoms, *Nature* **519**, 211 (2015).
 - 49 A. Mazurenko, C. S. Chiu, G. Ji, M. F. Parsons, M. Kanasz-Nagy, R. Schmidt, F. Grusdt, E. Demler, D. Greif, and M. Greiner, A cold-atom Fermi-Hubbard antiferromagnet, *Nature* **545**, 462 (2017).
 - 50 M. Greiner and S. Folling, Optical lattices, *Nature* **453**, 736 (2008).
 - 51 C. Sanner, E. J. Su, W. Huang, A. Keshet, J. Gillen, and W. Ketterle, Correlations and Pair Formation in a Repulsively Interacting Fermi Gas, *Phys. Rev. Lett.* **108**, 240404 (2012).
 - 52 Y. Ji, G. L. Schumacher, G. G. T. Assumpcao, J. Chen, J. T. Makinen, F. J. Vivanco, and N. Navon, Stability of the Repulsive Fermi Gas with Contact Interactions, *Phys. Rev. Lett.* **129**, 203402 (2022).
 - 53 M. S. Kim, M. C. Bennett, and M. C. Aronson, $\text{Yb}_2\text{Pt}_2\text{Pb}$: Magnetic frustration in the Shastry-Sutherland lattice, *Phys. Rev. B* **77**, 144425 (2008).
 - 54 M. Fujihala, K. Morita, R. Mole, S. Mitsuda, T. Tohyama, S.-i. Yano, D. Yu, S. Sota, T. Kuwai, A. Koda, H. Okabe,

- H. Lee, S. Itoh, T. Hawai, T. Masuda, H. Sagayama, A. Matsuo, K. Kindo, S. Ohira-Kawamura, and K. Nakajima, Gapless spin liquid in a square-kagome lattice antiferromagnet, *Nat. Commun.* **11**, 3429 (2020).
- ⁵⁵ C. Lee *et al.*, Random-singlet-like state emergent in $s = 5/2$ frustrated cubic lattice, *J. Korean Phys. Soc.* **84**, 151–157 (2024).
- ⁵⁶ R. Moessner and S. L. Sondhi, Resonating Valence Bond Phase in the Triangular Lattice Quantum Dimer Model, *Phys. Rev. Lett.* **86**, 1881 (2001).
- ⁵⁷ T. Itou, A. Oyamada, S. Maegawa, M. Tamura, and R. Kato, Quantum spin liquid in the spin-1/2 triangular antiferromagnet $\text{EtMe}_3\text{Sb}[\text{Pd}(\text{dmit})_2]_2$, *Phys. Rev. B* **77**, 104413 (2008).
- ⁵⁸ T. Arh, B. Sana, M. Pregelj, P. Khuntia, Z. Jaglicic, M. D. Le, P. K. Biswas, P. Manuel, L. Mangin-Thro, A. Ozarowski, and A. Zorko, The Ising triangular-lattice antiferromagnet neodymium heptatantalate as a quantum spin liquid candidate, *Nat. Mater.* **21**, 416 (2022).
- ⁵⁹ H. Bu, M. Ashtar, T. Shiroka, H. C. Walker, Z. Fu, J. Zhao, J. S. Gardner, G. Chen, Z. Tian, and H. Guo, Gapless triangular-lattice spin-liquid candidate $\text{PrZnAl}_{11}\text{O}_{19}$, *Phys. Rev. B* **106**, 134428 (2022).
- ⁶⁰ D. Bairwa, A. Bandyopadhyay, D. Adroja, G. B. G. Stenning, H. Luetkens, T. J. Hicken, J. A. Krieger, G. Cibin, M. Rotter, S. Rayaprol, P. D. Babu, and S. Elizabeth, Quantum spin liquid ground state in the rare-earth triangular antiferromagnet $\text{SmTa}_7\text{O}_{19}$, *Phys. Rev. B* **111**, 104413 (2025).
- ⁶¹ S. H. Lee, H. Kikuchi, Y. Qiu, B. Lake, Q. Huang, K. Habicht, and K. Kiefer, Quantum-spin-liquid states in the two-dimensional kagome antiferromagnets $\text{Zn}_x\text{Cu}_{4-x}(\text{OD})_6\text{Cl}_2$, *Nat. Mater.* **6**, 853 (2007).
- ⁶² J. S. Helton, K. Matan, M. P. Shores, E. A. Nytko, B. M. Bartlett, Y. Yoshida, Y. Takano, A. Suslov, Y. Qiu, J.-H. Chung, D. G. Nocera, and Y. S. Lee, Spin Dynamics of the Spin-1/2 Kagome Lattice Antiferromagnet $\text{ZnCu}_3(\text{OH})_6\text{Cl}_2$, *Phys. Rev. Lett.* **98**, 107204 (2007).
- ⁶³ P. Mendels and F. Bert, Quantum Kagome Antiferromagnet $\text{ZnCu}_3(\text{OH})_6\text{Cl}_2$, *J. Phys. Soc. Jpn.* **79**, 011001 (2010).
- ⁶⁴ F. Becca, L. F. Tocchio, and S. Sorella, Metal-insulator transition and strong-coupling spin liquid in the t - t' Hubbard model, *J. Phys.: Conf. Ser.* **145**, 012016 (2009).
- ⁶⁵ V. B. Shenoy, T. Gupta, H. R. Krishnamurthy, and T. V. Ramakrishnan, Long-range Coulomb interactions and nanoscale electronic inhomogeneities in correlated oxides, *Phys. Rev. B* **80**, 125121 (2009).
- ⁶⁶ Zs. Rak and D. W. Brenner, Exchange interactions and long-range magnetic order in the $(\text{Mg},\text{Co},\text{Cu},\text{Ni},\text{Zn})\text{O}$ entropy-stabilized oxide: A theoretical investigation, *J. Appl. Phys.* **127**, 185108 (2020).
- ⁶⁷ M. C. Gutzwiller, Effect of Correlation on the Ferromagnetism of Transition Metals, *Phys. Rev. Lett.* **10**, 159 (1963).
- ⁶⁸ J. Kanamori, Electron Correlation and Ferromagnetism of Transition Metals, *Prog. Theor. Phys.* **30**, 275 (1963).
- ⁶⁹ J. Hubbard and B. H. Flowers, Electron correlations in narrow energy bands III. An improved solution, *Proc. R. Soc. Lond. A* **281**, 401 (1964).
- ⁷⁰ H. Kondo and T. Moriya, On the Metal-Insulator Transition in a Two-Dimensional Hubbard Model, *J. Phys. Soc. Jpn.* **65**, 2559 (1996).
- ⁷¹ P. A. Igoshev and V. Yu. Irkhin, Metal-insulator transition and antiferromagnetism in the generalized Hubbard model: Treatment of correlation effects, *Phys. Rev. B* **104**, 045109 (2021).
- ⁷² J. E. Hirsch, Simulations of the three-dimensional Hubbard model: Half-filled band sector, *Phys. Rev. B* **35**, 1851 (1987).
- ⁷³ H. Q. Lin and J. E. Hirsch, Two-dimensional Hubbard model with nearest and next-nearest-neighbor hopping, *Phys. Rev. B* **35**, 3359 (1987).
- ⁷⁴ L. F. Tocchio, F. Becca, A. Parola, and S. Sorella, Role of backflow correlations for the nonmagnetic phase of the t - t' Hubbard model, *Phys. Rev. B* **78**, 041101 (2008).
- ⁷⁵ A. Mukherjee, N. D. Patel, S. Dong, S. Johnston, A. Moreo, and E. Dagotto, Testing the Monte Carlo–mean field approximation in the one-band Hubbard model, *Phys. Rev. B* **90**, 205133 (2014).
- ⁷⁶ A. Mukherjee, N. D. Patel, C. Bishop, and E. Dagotto, Parallelized traveling cluster approximation to study numerically spin-fermion models on large lattices, *Phys. Rev. E* **91**, 063303 (2015).
- ⁷⁷ R. Tiwari and P. Majumdar, Spectroscopic signatures of the Mott transition on the anisotropic triangular lattice, *Europhys. Lett.* **108**, 27007 (2014).
- ⁷⁸ S. Halder, S. Chakraborty, and K. Pradhan, Layer-resolved magnetotransport properties in antiferromagnetic/paramagnetic superlattices: Proximity effect induced antiferromagnetism in a paramagnetic metal, *Phys. Rev. B* **110**, 195147 (2024).
- ⁷⁹ J. K. Bidika, S. Mandal, Y. Shimakawa, K. Pradhan, and B. R. K. Nanda, Tunable magnetism in spin-half A -site ordered perovskites: $\text{CaCu}_3\text{B}_4\text{O}_{12}$, *Phys. Rev. B* **110**, 165161 (2024).
- ⁸⁰ S. Kumar and P. Majumdar, A travelling cluster approximation for lattice fermions strongly coupled to classical degrees of freedom, *Eur. Phys. J. B* **50**, 571 (2006).
- ⁸¹ S. Chakraborty, S. Halder, and K. Pradhan, Itinerant ferromagnetism in a spin-fermion model for diluted spin systems, *Phys. Rev. B* **108**, 165110 (2023).
- ⁸² S. Halder, S. Mandal and K. Pradhan, Microscopic study of interlayer magnetic coupling across the interface in antiferromagnetic bilayers, *Phys. Rev. B* **111**, 125149 (2025).
- ⁸³ P. R. C. Kent, M. Jarrell, T. A. Maier, and Th. Pruschke, Efficient calculation of the antiferromagnetic phase diagram of the three-dimensional Hubbard model, *Phys. Rev. B* **72**, 060411 (2005).
- ⁸⁴ A. A. Tsirlin, A. A. Belik, R. V. Shpanchenko, E. V. Antipov, E. Takayama-Muromachi, and H. Rosner, Frustrated spin- $\frac{1}{2}$ square lattice in the layered perovskite PbVO_3 , *Phys. Rev. B* **77**, 092402 (2008).
- ⁸⁵ L. Isaev, G. Ortiz, and J. Dukelsky, Hierarchical mean-field approach to the J_1 - J_2 Heisenberg model on a square lattice, *Phys. Rev. B* **79**, 024409 (2009).
- ⁸⁶ K. Majumdar and T. Datta, Zero temperature phases of the frustrated J_1 - J_2 antiferromagnetic spin-1/2 Heisenberg model on a simple cubic lattice, *J. Stat. Phys.* **139**, 714–726 (2010).
- ⁸⁷ H. C. Jiang, H. Yao, and L. Balents, Spin liquid ground state of the spin- $\frac{1}{2}$ square J_1 - J_2 Heisenberg model, *Phys. Rev. B* **86**, 024424 (2012).
- ⁸⁸ W. J. Hu, F. Becca, A. Parola, and S. Sorella, Direct evidence for a gapless Z_2 spin liquid by frustrating Néel antiferromagnetism, *Phys. Rev. B* **88**, 060402 (2013).
- ⁸⁹ S.-S. Gong, W. Zhu, D. N. Sheng, O. I. Motrunich, and M. P. A. Fisher, Plaquette ordered phase and quantum phase diagram in the spin- $\frac{1}{2}$ J_1 - J_2 square Heisenberg model,

Phys. Rev. Lett. **113**, 027201 (2014).

⁹⁰ G. D. Mahan, *Many-Particle Physics*, (Springer US, Boston, MA, 2000), pp. 499–577.

⁹¹ S. Kumar and P. Majumdar, Anti-localisation to strong lo-

calisation: The interplay of magnetic scattering and structural disorder, *Europhys. Lett.* **65**, 75 (2004).